

TotalVibeSegmentator: Full Body MRI Segmentation for the NAKO and UK Biobank

- Robert Graf* M. Sc. (1,2)
- Paul Platzek m. d. (1)
- Dr. Evamaria Olga Riedel (1)
- Dr. Constanze Ramschütz (1)
- Sophie Starck M. Sc (2)
- Hendrik K. Möller M. Sc (1,2)
- Matan Atad M. Sc (1,2)
- Prof. Dr. Henry Völzke (4)
- PD Robin Bülow (3)
- Prof. Dr. Carsten Oliver Schmidt (4)
- Prof. Julia Rüdibusch (4)
- Dr. Matthias Jung (5)
- Dr. Marco Reisert (5)
- PD Jakob Weiss (5)
- PD Maximilian T. Löffler (5,1)
- Prof. Dr. Fabian Bamberg (5)
- Prof. Benedikt Wiestler (1),
- Dr. Johannes C. Paetzold (6)
- Prof. Dr. Daniel Rueckert (6,2)
- Prof. Dr. Jan Stefan Kirschke (1)

*First author / corresponding author

1. Department of Diagnostic and Interventional Neuroradiology, School of Medicine, Technical University of Munich
Neuro-Kopf-Zentrum
Ismaninger Str. 22
81675 München, Germany
2. Institut für KI und Informatik in der Medizin, Klinikum rechts der Isar
Technical University of Munich
Neuro-Kopf-Zentrum
Ismaninger Str. 22
81675 München, Germany
3. Institute for Diagnostic Radiology and Neuroradiology
University Medicine Greifswald
Ferdinand-Sauerbruch-Straße
17475 Greifswald, Germany
4. Institut für Community Medicine, Abteilung SHIP-KEF,
University Medicine Greifswald,
Walter Rathenau Str. 48, 5. Etage
17475 Greifswald, Germany
5. Department of Diagnostic and Interventional Radiology, University Medical Center Freiburg,
Faculty of Medicine,
University of Freiburg
Hugstetter Str. 55
79106 Freiburg, Germany
6. Department of Computing
Imperial College London
Room 568, Huxley Building
180 Queen's Gate
London SW7 2AZ, UK

Article Type: Original Research

Summary statement:

We developed an MR segmentation model, with special focus on Vibe images, with 71 different segmentation classes.

Key Points:

- Our method achieves the highest number of segmentation classes to date for MRI full torso segmentation, covering 71 structures.
- We trained our model using 13 different contrast types, maintaining a fixed resolution, across 1703 series.
- Our segmentations accurately touch and delineate the true transition boundaries of anatomical structures.

Key Words:

Segmentation, Torso, VIBE, MRI, Biobank

Abbreviations:

VIBE	volumetric interpolated breath-hold examination
NAKO	German National Cohort (NAKO Gesundheitsstudie)
UKBB	UK-Biobank
SHIP	Study of Health in Pomerania
FOV	field of view
MEVIBE	multi echo vibe (6-point Dixon)
Haste	Half Fourier-acquisition single-shot turbo spin echo
T2w	T2-weighted

Abstract

This study presents a publicly available deep learning-based torso segmentation network tailored for large epidemiology datasets, particularly volumetric interpolated breath-hold examination (VIBE) images, using nnUNet. We refined preliminary segmentations from various networks and retrained a nnUNet model iteratively. A subset of German National Cohort (NAKO) and UK Biobank data (training: 1704 series, 158 subjects; testing: 12 subjects) was used to segment 71 structures, including 20 organs, 10 muscles, 19 vessels, 16 bones, and body composition, segmenting most of the torso. The model achieved an average Dice score of 0.92 ± 0.04 on internal test data. For external validation we used existing automatic abdominal organ segmentations, independent ground truths and the out-of-distribution Amos data. On the out-of-distribution Amos dataset, it achieved a Dice score of 0.76 ± 0.19 . This segmentation network provides the most detailed publicly available model for full torso segmentation on VIBE images.

Introduction



Figure 1: 3D rendering of our segmentations for NAKO and UK-Biobank subjects on Volumetric Interpolated Breath-hold Examination (VIBE) water image. A) bones, intervertebral disc, and costal cartilages; B) digestion; C) lung-lobes, and trachea; D) muscles; E) organs; F) vessels; G) spinal cord and canal; H) subcutaneous fat, muscle (other) and inner fat. NAKO - German National Cohort; VIBE - Volumetric Interpolated Breath-hold Examination;

Segmentation for MRI is useful for both clinical purposes and epidemiological studies. Clinically, it may aid in streamlining diagnosis, treatment planning, and personalized healthcare. In epidemiological research, segmentation enables large-scale analysis of

population health, facilitating the computation of health parameters across diverse demographics¹.

The Volumetric Interpolated Breath-hold Examination (VIBE) employs a two-point Dixon sequence to separate water and fat content in MRI images². Large epidemiological studies in Europe, such as the German National Cohort (NAKO)³, the UK-Biobank (UKBB)⁴, and the Study of Health in Pomerania (SHIP)⁵ have utilized VIBE for comprehensive torso imaging. Both UKBB and NAKO datasets feature full torso images, with only the head and parts of the arms and legs outside the field of view (FOV).

Recent advancements, such as the release of TotalSegmentator⁶, have provided comprehensive torso segmentation for CT scans, promising significant benefits for future research. We extended this segmentation capability to VIBE MR images and others, enabling the automated evaluation of large full-body image collections from NAKO and UKBB. Our approach combines recent works in spine segmentation in MRI⁷⁻⁹, domain adaptation to use the TotalSegmentator⁶ on MR images, and existing MR-specific annotations by Jung et al.¹⁰. The resulting portfolio of regions encompasses 71 distinct semantic segmentation classes plus 22 instance vertebra classes (C3 to L5). By automating the segmentation of these diverse anatomical structures, we aim to provide a robust tool for both clinical applications and large-scale epidemiological research, facilitating the extraction of meaningful biomarkers and the advancement of AI-based reporting and analysis tools e.g., to be used in early cancer detection^{11,12}. Our segmentations aim to closely produce the same semantic labels as TotalSegmentator, enabling structural comparison between CT and MR images of the same subject. Given that NAKO consists of different anatomically aligned image datasets, we extended our approach to other MR contrasts. These include T2-weighted HASTE (torso), proton density (hip area), six-point Dixon technique (lower torso), and sagittal T2-weighted turbo spin echo (spine only). We support the open-source mission of TotalSegmentator and freely publish our trained nnUNet¹³ weights for full torso segmentation on VIBE and other MRI data: (Github <https://github.com/robert-graf/TotalVibeSegmentator>).

This study creates a model for full torso segmentation on VIBE images. This enables automatic analyses of large epidemiological studies for norm-value generation, registration, masking, and outlier detection.

Materials and Methods

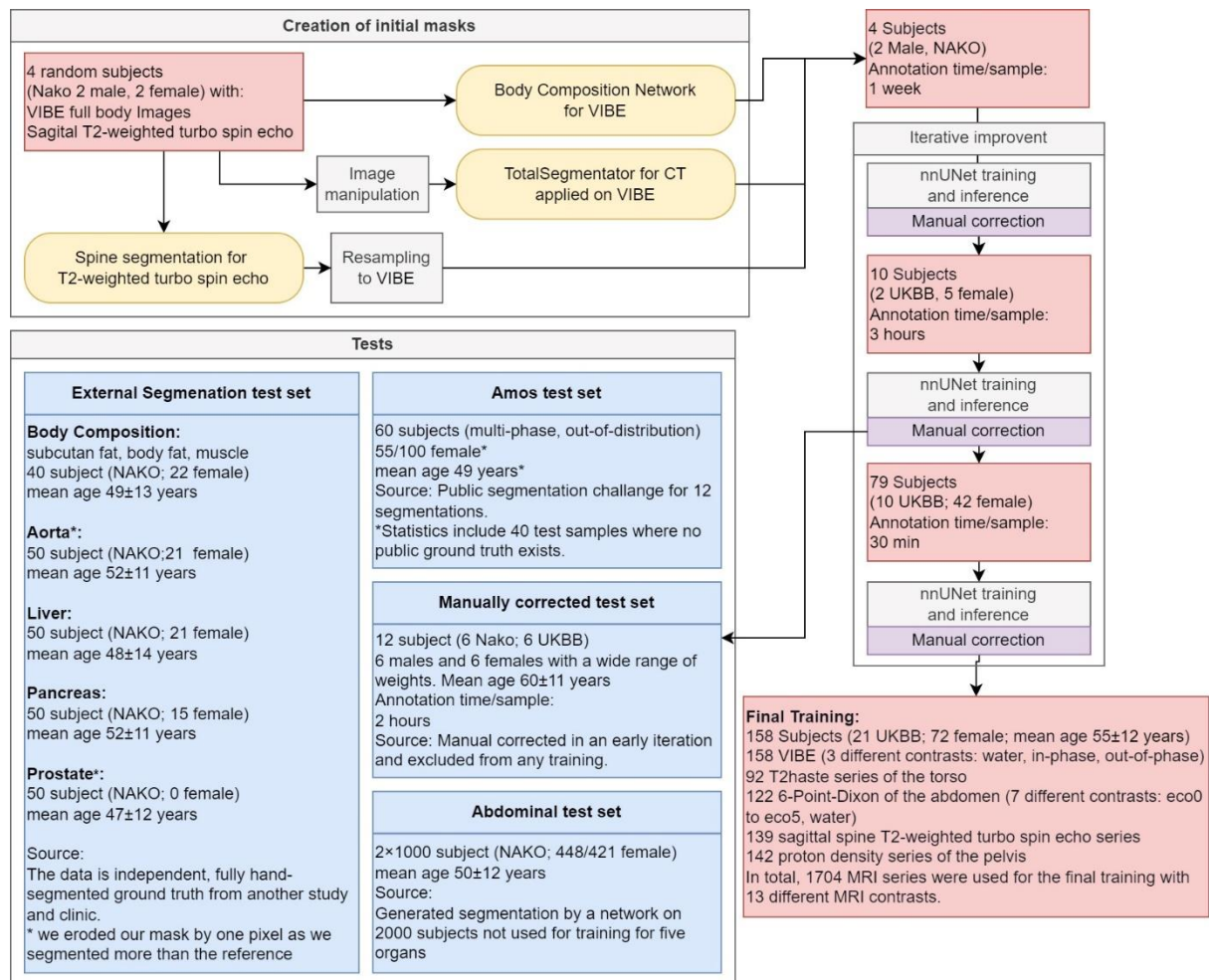


Figure 2: We generate initial masks from different sources (yellow) and then iteratively increase the training dataset (red). We use four test sets (blue): A manually corrected test set, the Amos dataset, fully independent human annotated segmentation from another clinic and a large automatic test set from abdominal organ segmentation. NAKO - German National Cohort; UKBB - UK-Biobank; VIBE - Volumetric Interpolated Breath-hold Examination;

This retrospective study uses a random subset of the full-body VIBE data from NAKO, acquired at Augsburg and Neubrandenburg, along with data from UKBB for training and evaluation. Ethical approval for data collection was obtained from the respective ethics committees, and

informed consent was obtained. Additionally, ethical approval was obtained from our local ethics committee.

The NAKO VIBE images were acquired in four stacks in axial orientation, with an in-plane resolution of 1.4 mm and a through-plane resolution of 3 mm³. In comparison, the UKBB VIBE images were obtained with a lower in-plane resolution of 2.2 mm and 3 mm slice thickness⁴. Our network was trained on the native resolution of the NAKO images, with the UKBB images upsampled to match this resolution. NAKO images were stitched with a updated stitching tool¹⁴, while UKBB images were stitched using the stitching tool from Glocker et al.¹⁵. Data selection was random and only images with motion artifacts were removed. We use additional sequences from the NAKO with limited field of view (FOV) to enable segmentation on multiple MR sequence types.

Our final segmentation model included 71 semantic tissue classes. We also provide individual vertebra segmentation as a separate model. Known issues with vertebra instance segmentation with nnUNet and the reliability of this model are discussed in the supplemental material. For the spine we separated vertebrae in vertebral bodies and posterior elements, and added five additional semantic regions (subcutaneous fat, muscle (other), inner fat, intervertebral disc, and spinal canal). Due to challenges in annotation, we opted not to segment ribs and merged the colon and small bowel into a single "intestine" label. We found the contrast not strong enough to confidently delineate them in VIBE images for both classes. Skull and brain segmentation are omitted because they fall outside the FOV and there are already many well-established algorithms available for skull segmentation in MRI^{16,17}. Additionally, structures like the patella, fibula, tibia, ulna, and radius are rare and only partially captured in the FOV of the NAKO and UKBB datasets, hence categorized into a collective class labeled "bone (other)." We did not reproduce the cysts classes as pathologies are out of scope for this work and are highly underrepresented in UKBB and NAKO compared to a clinical dataset. With the CT TotalSegmentator we can match structures in MRI and CT.

In total, we only miss 4 class types that are segmented in the publicly available CT TotalSegmentator (version 2): ribs, brain, skull, and kidney cysts classes.

Ground truth generation.

As it is unfeasible to annotate full-torso images completely manually to obtain a baseline, we took an iterative, stepwise approach, combining available segmentation models with existing ground truth annotations and several iterations of manual refinements (Figure 1). We used the existing segmentation from CT TotalSegmentator and body-composition as a reference standard. The segmentation refinement process involved four radiologists utilizing ITK-Snap version 3.8.0¹⁸. Three radiologists with 2-3 years of experience conducted the initial segmentation correction under the supervision of a senior radiologist with 22 years of experience. We used three sources for the initial segmentation proposal: The CT TotalSegmentator on manipulated water images, SPINEPS T2w turbo spine echo for vertebra segmentation^{7,8}, and body composition network by Jung et al.¹⁰ to segment the additional subcutaneous fat, muscle (other) and inner fat. Details for the initial ground truth segmentation can be found in the supplemental material. We utilized an iterative approach similar to TotalSegmentator⁶, Verse¹⁹, and AbdomenAtlas-8K²⁰ to increase the number of training images. This iterative process involves correcting predicted segmentation masks and retraining the network until achieving a point of diminishing return. After obtaining the first 4 segmentations, we iteratively trained a nnUNet¹³. After each retraining, we again corrected the new segmentation masks to increase the training dataset. We implemented training and data augmentation strategies described in the supplemental material to increase generalizability, prevent under-segmentation, reduce false predictions and speed up inference time. The final training was done on 1704 MRI with 13 different contrasts from 158 subjects. See Figure 1 for details.

Evaluations

For external evaluation, we utilized the inference of the abdominal networks as outlined in Kart et al.^{21,22}, independent ground truths from another group working on the NAKO data, and out-of-distribution data from the Amos dataset²³. We internally validated our model on 12 manually corrected images, evenly distributed between NAKO and UKBB datasets (50% female),

selected to cover a wide range of body weights per sex and dataset. Quality metrics were assessed using the Dice score.

Statistical Analysis

For evaluation, we utilized the Scipy²⁴ and Panoptica Python²⁵ packages. Nonparametric bootstrapping of 10,000 iterations was utilized to compute 95% confidence intervals (CIs) and Wilcoxon rank-sum test for computing statistical significance.

Results

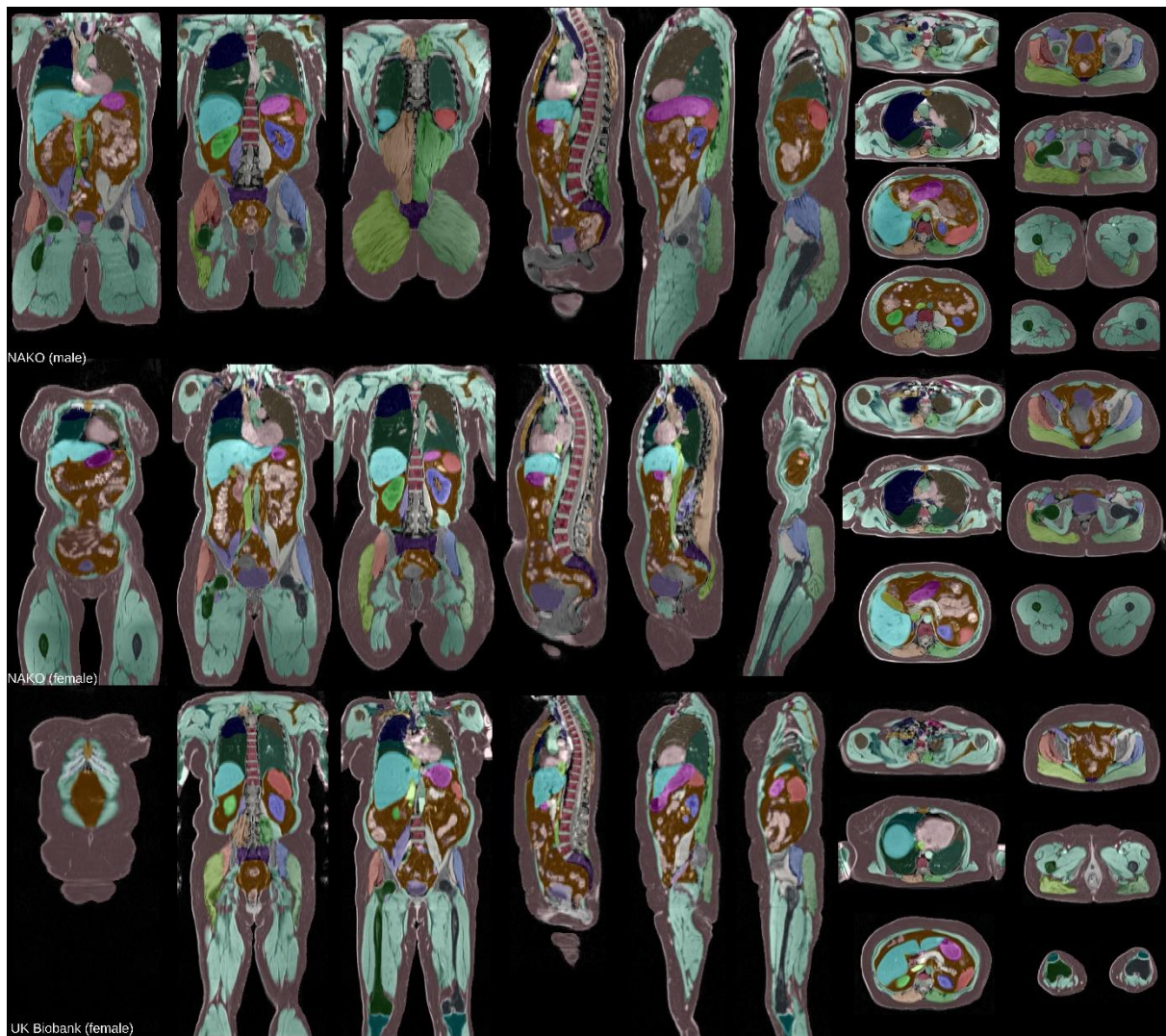


Figure 3: Segmentation for three random VIBE images on the NAKO and UK Biobank. NAKO - German National Cohort; VIBE -Volumetric Interpolated Breath-hold Examination;

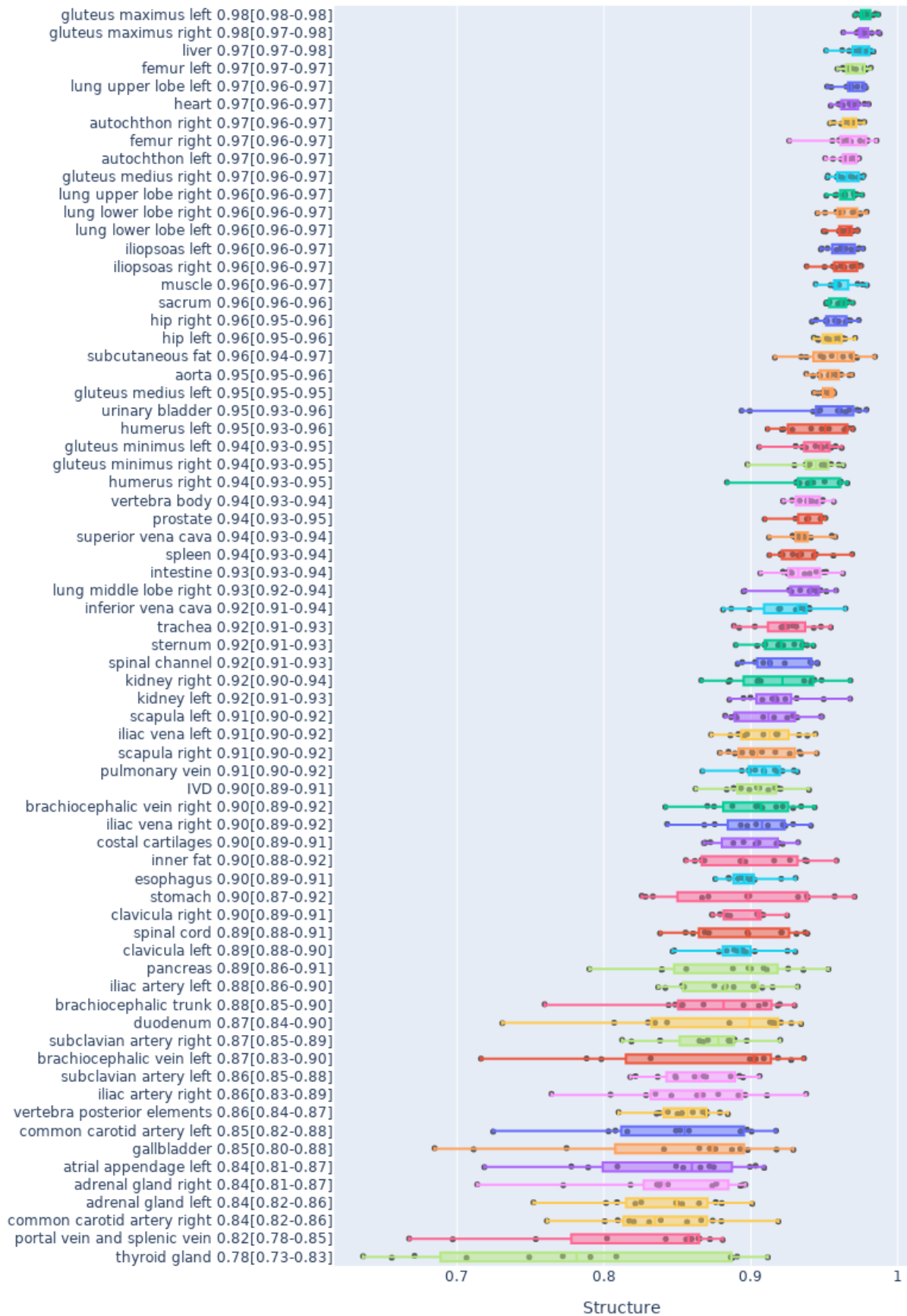


Figure 4: Test set. Dice scores over all classes compared on repaired and predicted VIBE on the 12 NAKO and UK Biobank images. The box-plot center is the mean, and bars define standard differences. NAKO - German National Cohort, VIBE -Volumetric Interpolated Breath-hold Examination;

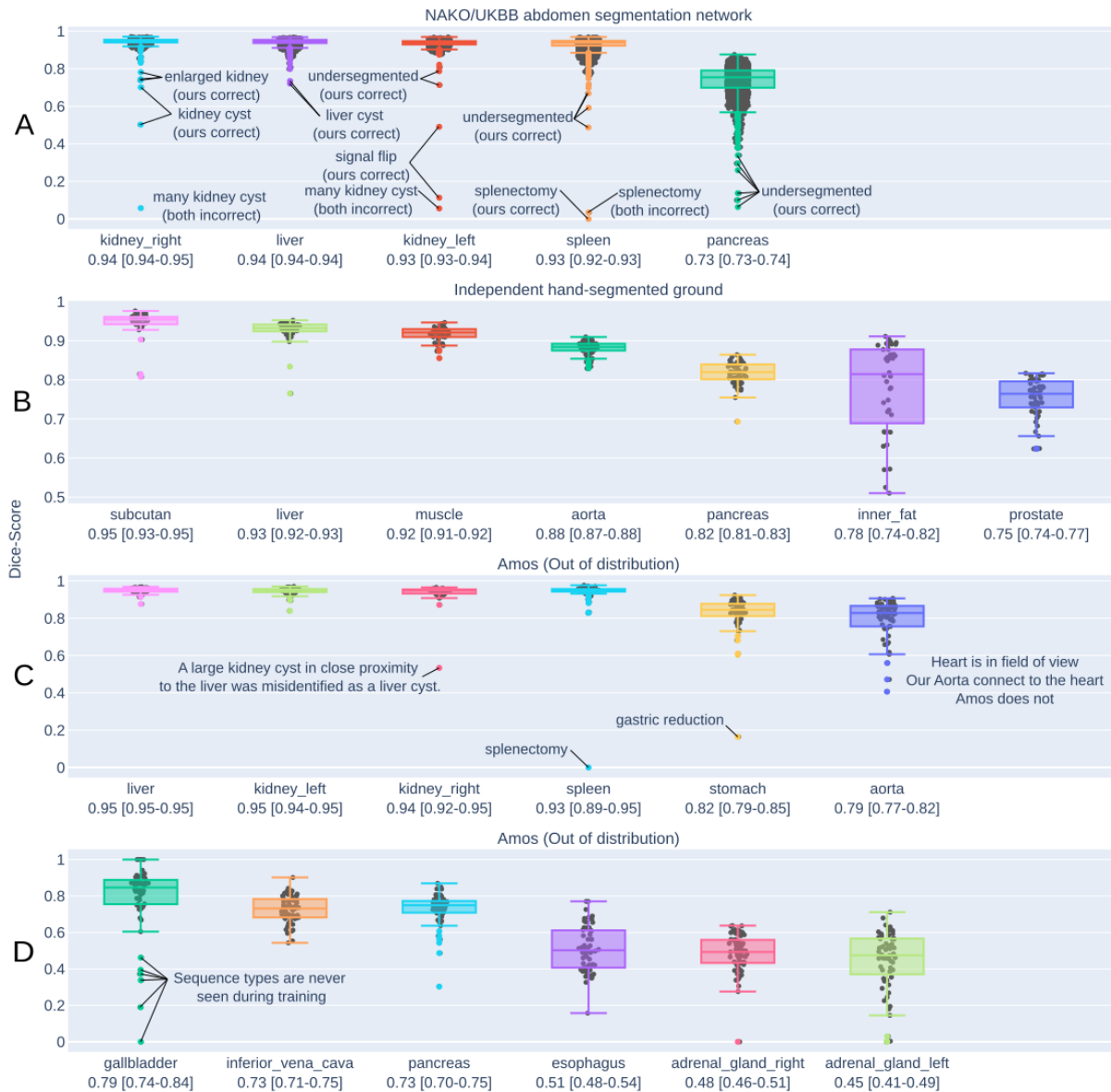


Figure 5: External Validation. A) Dice scores over 1000 test samples compared to the prediction of the NAKO/UKBB abdomen segmentation network. Although without manual reference masks, this shows the agreement between both approaches. The source of outliers can be caused by either of the networks. B) Independent handmade ground truths from another clinic on NAKO images. C) and D) Amos dataset with varying resolution and MR sequences. The box-plot center is the mean, and bars define standard differences. NAKO - German National Cohort; VIBE - Volumetric Interpolated Breath-hold Examination;

Internal Evaluations

Our objective was to maximize the fill with semantic labels, excluding the reproductive organs, and tissue around lungs and spine. See Figure 3. On our internal test set, the average volumetric Dice score across all classes was 0.92 ± 0.04 . Individual scores are detailed in Figure

4 and Table 1. Structures with low contrast, high variability, and small size exhibited the lowest Dice scores. For instance, the adrenal gland is too small to be resolved at the given VIBE image resolution, highlighting the area rather than delineating the exact structure. Similarly, the thyroid gland, pancreas, and "portal vein and splenic vein" lack clear delineations. The gallbladder's size varies significantly, sometimes being very small, which can result in large score drops due to minor errors. The average symmetric surface distance is reported in Supplementary Figure 3.

External Evaluations on NAKO data

In Figure 5, we show all Dice scores from all three external evaluations. Our segmentation closely aligns with abdominal segmentation by Kart et al.^{21,22} for the liver, kidney, and spleen. The pancreas, however, presents challenges in achieving consistent segmentation, which is already reported by Kart et al.^{21,22}.

We received independently generated ground truths of liver, aorta, pancreas, and prostate for VIBE images on the NAKO from an independent clinic and study from Freiburg and the ground truth of the body-composition by Jung et al.¹⁰. Our body-composition intentionally added arms, legs, and parts of the shoulder area. Further, we joined the edges between structures to fill holes in the segmentation, leading to a slight shift from the original ground truth, most noticeable in the inner fat segmentation (0.78 Dice; CI: [0.74, 0.82]). We measured the Dice of the general muscle (0.92 Dice; CI: [0.91, 0.92]) and subcutaneous fat (0.95 Dice; CI: [0.93, 0.95]), after we masked the newly created arm and leg regions away. Our segmentation of the aorta (0.88 Dice; CI: [0.87, 0.88]) included the ascendent aorta as well as the vessel wall, unlike the reference that just segmented the lumen of the aortic arch and the descendent part. The liver (0.93 Dice; CI: [0.92, 0.93]) and pancreas (0.82 Dice; CI: [0.81, 0.83]) Dice scores were consistent with other references. The prostate segmentation (0.75 Dice; CI: [0.74, 0.77]) is larger than the manual segmentation.

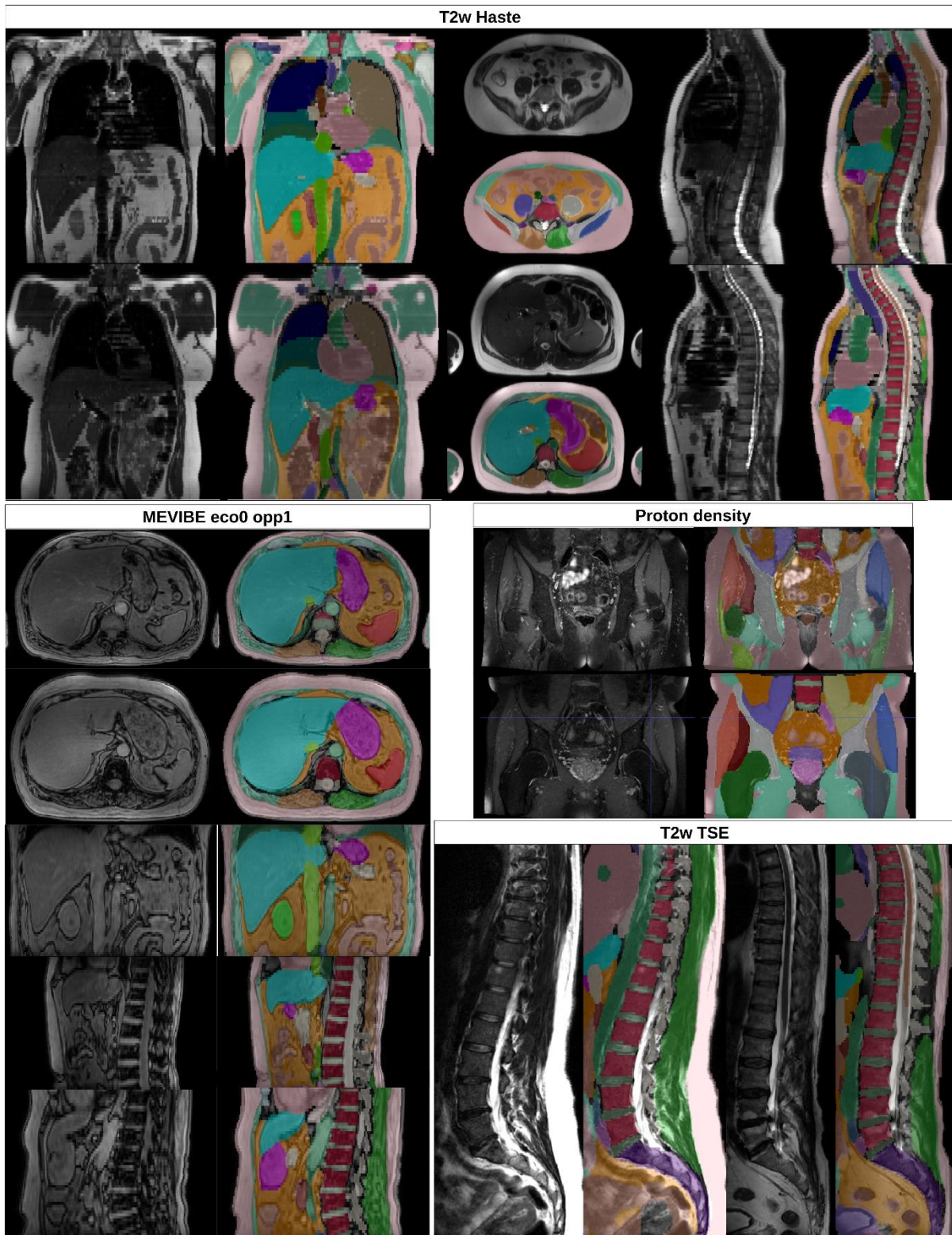


Figure 6: Running our segmentation on other NAKO sequence types. We used for training resampled ground truth segmentation to the other sequences. T2w Haste (Half Fourier-acquisition single-shot turbo spin echo) works best even with the breathing and heart movement of the images. MEVIBE (multi echo vibe) has out of phase images with clear delineations like the “eco0 opp1” signal. The proton density and T2w TSE (turbo spin echo) has signal drops in the NAKO, producing errors where the signal drop is too strong.

External Evaluations on out-of-distribution data

We also trained on other resampled sequences, as shown in Supplemental Figure 1. Using the Amos dataset²³, we demonstrated that our segmentation model can handle MR modalities not seen during training, such as contrast-enhanced images, or coronal images. We achieved a Dice score of 0.76 ± 0.19 , despite not training our model on some of the MR sequences, different resolutions, and varying delineation definitions. Instances, where the spleen and gallbladder were not segmented in Amos, resulted in some 0 scores, as our segmentation model produced small segments where they should be. One subject had a splenectomy and gastric reduction, which our model failed to recognize. The outlier in the aorta segmentation is due to our model segmenting the section between the heart and the direction inversion, unlike the Amos model. Gallbladder segmentation (0.79 Dice; CI: [0.74, 0.84]) showed the highest variability, reflecting poor agreement for MR sequence types not included in the training set. Our esophagus segmentation (0.51 Dice; CI: [0.48, 0.54]) is roughly twice as thick as the Amos segmentation because we segment both the lumen and the muscular tissue. In the VIBE images, the adrenal glands are barely visible due to the sequence type and resolution (0.48/0.45 Dice). In contrast, the adrenal gland edges are clearly visible in some Amos images, but our model has not been trained on such images. Our focus was the evaluation of VIBE images and leave out the other modalities for brevity. Visual examples can be seen in Figure 6

Failure analysis

We used the second last network and the abdominal segmentation network^{21,22} to find failure cases to include them in the training. We segmented 1,000 images (448 female, mean age 50) using the abdominal segmentation network^{21,22} and compared our second last model's output. We inspected 40 outliers where at least one segmentation was two standard deviations below the mean Dice score. Four images had a water/fat inversion error in the MR signal. Our segmentation was robust to these errors, producing only minor inaccuracies at the inversion lines. In addition to these issues, both models produced errors for horseshoe kidneys, liver

and kidney cysts, and abnormally large kidneys and spleens, which were only partially segmented. Our model produced faults in 12 out of 40 cases, while the abdominal segmentation method^{21,22} produced faults in 35 out of 40 cases. We counted a segmentation as faulty if at least 10% of the organ was missing or over-segmented. We corrected these and added them to the final training. We repeated the experiment with another 1,000 images (421 female, mean age 50). Results showed that the model was more robust to cyst and size changes, and only extreme cases caused segmentation errors after including other images with pathologies. We did not find issues with our pancreas segmentation in both tests, but observed that the abdominal segmentation network^{21,22} has issues with pancreases if the person has larger amounts of body fat. We marked the outlier of the second test in Figure 5. Known failure cases include subjects with additional or displaced organs, such as with kidneys, or unseen pathologies. Similar issues occur with the head, feet, hands, and forearms, as these are outside the field of view of our training data. We have not observed segmentation errors in bone and lung segmentation in our healthy subjects so far.

Other Methods

This study was independently conducted while other “MRI TotalSegmentator” approaches were developed^{26–28}. In Figure 7 and Table 2 we highlight the differences between these approaches. In Table 1 we computed Dice scores on our internal test set on two networks (Akinci D’Antonoli et al.²⁶ and Häntze et al.²⁷). The average Dice score of 43 shared structures is 0.68 ± 0.17 by Akinci D’Antonoli et al., to ours with 0.92 ± 0.09 ($p < 0.001$). For Häntze et al. 36 shared structures had an average Dice of 0.76 ± 0.11 compared to 0.93 ± 0.05 ($p < 0.001$) on our internal test data. These lower Dice scores in D’Antonoli and Häntze can predominantly be explained by differences in the segmentation borders: they keep a small distance to the organ’s surface to exclude partial volume effects and ensure a correct quantification of the organ’s signal intensity. We try to match the border of the organ to exactly reveal the volume. This limits the interpretability of this Dice comparison. Example segmentations are shown in Figure 7. The model by Zhuang et al.²⁸ was not available at the time of writing.

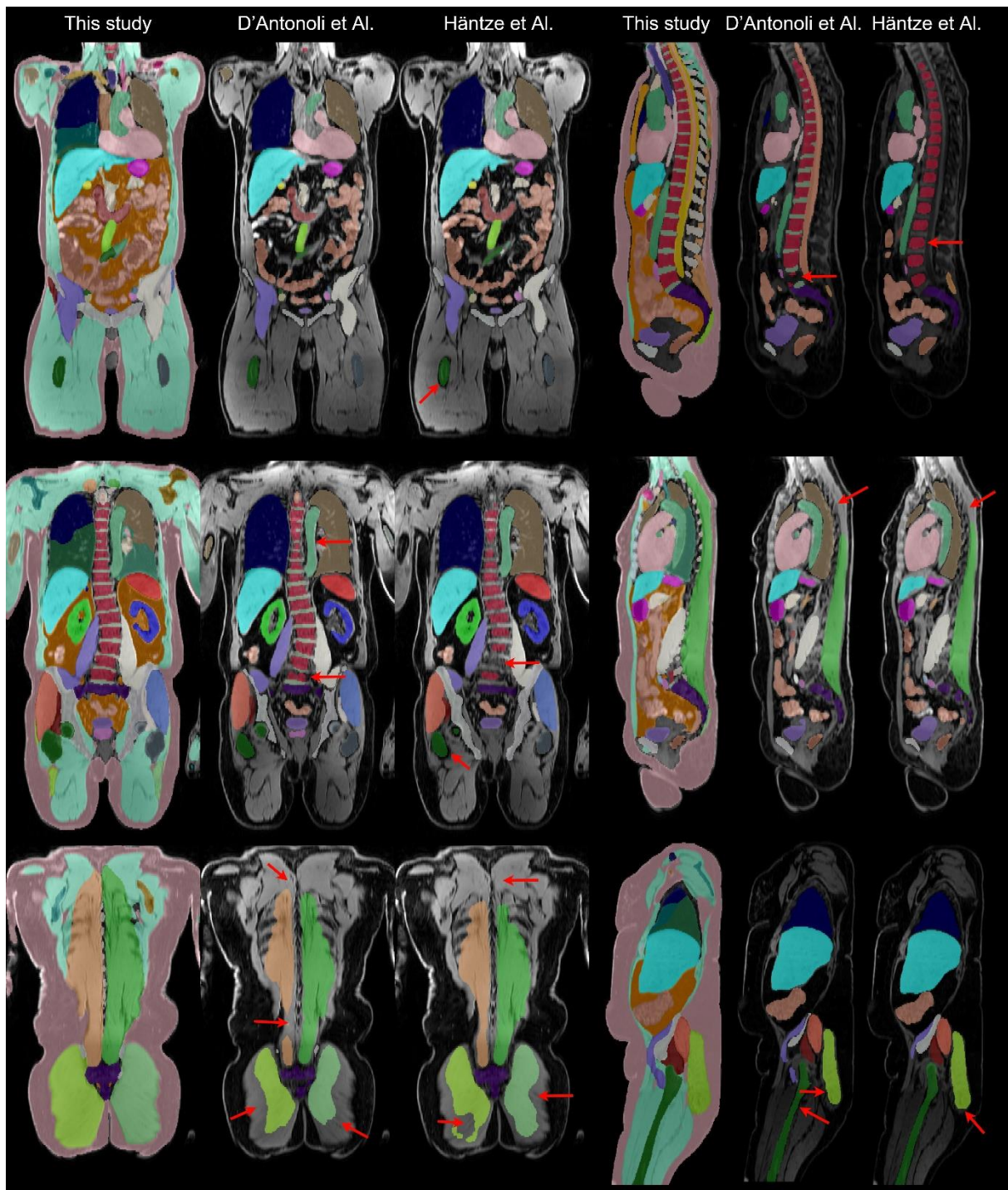


Figure 7: Visual comparison of D'Antonoli et Al. and Häntze et Al. and this study in coronal and sagittal slices of VIBE images from NAKO data set. Our segmentation does not under-segment structures like muscles and bones and follows the existing lines better. In the case of bone, the dark line belongs to the bone, as it is dense bone with low proton signal. We marked examples of under-segmentation with red arrows. We show only labels that match ours. Our lung segmentation has 5 lung lobes instead of 2 sides. We have additional heart vessels, additional bones in the upper body and body-composition labels. NAKO - German National Cohort; VIBE - Volumetric Interpolated Breath-hold Examination

Discussion

In this study, we developed a comprehensive full-torso segmentation model incorporating 71 semantic segmentation labels for the NAKO and UKBB VIBE images. Specifically, our model achieves detailed segmentation of 20 organs, 10 muscles, 19 vessels, 16 bones, and 3 additional spinal structures (intervertebral disc, spinal cord, and spinal canal). Moreover, we include body composition segmentation into three classes, delineating different fat compartments and body parts. Additionally, we provide full vertebra instance segmentation on the same datasets. This MRI-based total segmentation on VIBE images offers significant potential for medical imaging by providing detailed anatomical insights and facilitating advanced research applications⁶. Trained on various aligned sequences, our model demonstrates versatility across 13 different MRI contrasts. Previous studies have highlighted the efficacy of segmentation techniques within the NAKO cohort, such as abdominal organ segmentation and quality control in a large sample of 20,000 participants^{21,22}. Our model extends previous capabilities of whole-body segmentation models to include detailed fat and muscle tissues, building on the work by Jung et al.¹⁰ on VIBE images. This segmentation facilitates fat distribution estimation, akin to the methods employed by Somasundaram and Wu et al. on 6-point Dixon images²⁹.

Independent of this work, other full MR segmentations have been developed^{26–28}. In addition to completely different training datasets, our approach features several key differences. By including body composition, we can classify most pixels into a specific category, which stabilizes our segmentation. In some cases, our approach is unique in incorporating most border regions, such as those around bones, and identifying contact points of muscles with other segments. With 71 tissue classes plus additional vertebra instance segmentation, our model offers the most comprehensive segmentation to date. Although our model shows slightly lower numerical performance on the Amos dataset²³, it provides more segmentations over a larger FOV. To make our approach fully complementary to other existing segmentation

approaches, we did not include Amos in our training. Our model tends to segment the border and supporting tissue in vessels, the gallbladder, and the stomach, generally resulting in over-segmentation rather than under-segmentation. In contrast, the Amos segmentation tends to under-segment, particularly for structures like vessel walls. We attribute larger performance gaps, that are not the result of diverging definition, to our annotations being based solely on a specific set of FOVs and MRI series. In contrast, other studies use sequences not included in our training, such as contrast-enhanced or coronal-acquired images. These advancements in MRI segmentation highlight the rapid progress in the field. We anticipate the imminent release of multiple multi-segmentation models, which will provide the scientific community with independent frameworks for abdominal segmentation across various modalities. This will enable cross-validation, enhance the robustness of segmentation techniques, and facilitate valuable comparative analyses.

Despite its advantages, the NAKO and UKBB datasets have certain limitations. While they offer a large FOV and high resolution, they contain fewer anomalies, potentially limiting the diversity of pathological cases in the training data. We omitted pathology segmentation as it is outside the scope of this work. For digestive organs, delineation is more challenging in VIBE images compared to T1-weighted fast spin echo images with a contrast agent, due to minimal contrast changes in VIBE. Although the availability of HASTE, PD, and MEVIBE sequences is a notable benefit, challenges remain. For instance, very small structures in the UKBB dataset, such as the thyroid gland, are difficult to segment due to being nearly lost in image noise. Additionally, the arms, legs, and head are only partially visible in all datasets, leading to undefined segmentation behavior in these regions and necessitating a separate improvement dataset. Feedback from radiologists indicates that our sacrum segmentation includes non-bone tissue, and our thyroid gland segmentation, while following delineation visible in VIBE MRI, results in discrepancies compared to CT segmentation in a 3D view. These insights highlight the need for further refinement and validation of our segmentation approach.

In conclusion, our work significantly advances the field of MRI segmentation by providing a detailed and refined approach to full torso segmentation. By addressing limitations and overcoming issues such as right-left mis-segmentation, we aim to enhance the capabilities of MRI segmentation and support its application in diverse clinical and research settings.

Data Availability & Code availability

The underlying code and pretrained models for this study are available on Github and can be accessed via <https://github.com/robert-graf/TotalVibeSegmentator> under the Apache-2.0 license. The MRI data of the manual corrected segmentation that support the findings of this study are available from NAKO and UKBB but restrictions apply to the availability of these data, which were used under license for the current study, and so are not publicly available. Data are however available from the authors upon reasonable request, if NAKO or UKBB access exists.

References

1. Gillies, R. J., Kinahan, P. E. & Hricak, H. Radiomics: images are more than pictures, they are data. *Radiology* **278**, 563–577 (2016).
2. Koh, E., Walton, E. R. & Watson, P. VIBE MRI: an alternative to CT in the imaging of sports-related osseous pathology? *The British Journal of Radiology* **91**, 20170815 (2018).
3. Bamberg, F. *et al.* Whole-body MR imaging in the German National Cohort: rationale, design, and technical background. *Radiology* **277**, 206–220 (2015).
4. Allen, N. *et al.* UK Biobank: Current status and what it means for epidemiology. *Health Policy Technol. (HPT)* **1**, 123–126 (2012).
5. John, U. *et al.* Study of Health In Pomerania (SHIP): a health examination survey in an east German region: objectives and design. *Sozial-und Präventivmedizin* **46**, 186–194 (2001).
6. Wasserthal, J. *et al.* Totalsegmentator: Robust segmentation of 104 anatomic structures in ct images. *Radiology: Artificial Intelligence* **5**, (2023).
7. Graf, R. *et al.* Denoising diffusion-based MRI to CT image translation enables automated spinal segmentation. *European Radiology Experimental* **7**, 70 (2023).
8. Möller, H. *et al.* SPINEPS—Automatic Whole Spine Segmentation of T2-weighted MR images using a Two-Phase Approach to Multi-class Semantic and Instance Segmentation. *arXiv preprint arXiv:2402.16368* (2024).
9. Streckenbach, F. *et al.* Application of a Deep Learning Approach to Analyze Large-Scale MRI Data of the Spine. in *Healthcare* vol. 10 2132 (MDPI, 2022).
10. Jung, M. *et al.* Deep learning to predict mortality from whole-body magnetic resonance imaging in the general population.
11. Mikdadi, D. *et al.* Applications of artificial intelligence (AI) in ovarian cancer, pancreatic cancer, and image biomarker discovery. *Cancer Biomarkers* **33**, 173–184 (2022).
12. Prelaj, A. *et al.* Artificial intelligence for predictive biomarker discovery in immuno-oncology: A systematic review. *Annals of Oncology* (2023).

13. Isensee, F., Jaeger, P. F., Kohl, S. A., Petersen, J. & Maier-Hein, K. H. nnU-Net: a self-configuring method for deep learning-based biomedical image segmentation. *Nature methods* **18**, 203–211 (2021).
14. Graf, R. *et al.* Generating synthetic high-resolution spinal STIR and T1w images from T2w FSE and low-resolution axial Dixon. *European Radiology* (2024) doi:10.1007/s00330-024-11047-1.
15. Glocker, B. *et al.* MRI composing for whole body imaging. in *Bildverarbeitung für die Medizin 2009: Algorithmen—Systeme—Anwendungen Proceedings des Workshops vom 22. bis 25. März 2009 in Heidelberg* 420–424 (Springer, 2009).
16. Reuter, M., Schmansky, N. J., Rosas, H. D. & Fischl, B. Within-subject template estimation for unbiased longitudinal image analysis. *Neuroimage* **61**, 1402–1418 (2012).
17. Akkus, Z., Galimzianova, A., Hoogi, A., Rubin, D. L. & Erickson, B. J. Deep learning for brain MRI segmentation: state of the art and future directions. *Journal of digital imaging* **30**, 449–459 (2017).
18. Yushkevich, P. A. *et al.* User-Guided 3D Active Contour Segmentation of Anatomical Structures: Significantly Improved Efficiency and Reliability. *Neuroimage* **31**, 1116–1128 (2006).
19. Sekuboyina, A. *et al.* VerSe: a vertebrae labelling and segmentation benchmark for multi-detector CT images. *Medical image analysis* **73**, 102166 (2021).
20. Qu, C. *et al.* Abdomenatlas-8k: Annotating 8,000 CT volumes for multi-organ segmentation in three weeks. *Advances in Neural Information Processing Systems* **36**, (2024).
21. Kart, T. *et al.* Automated imaging-based abdominal organ segmentation and quality control in 20,000 participants of the UK Biobank and German National Cohort Studies. *Scientific Reports* **12**, 18733 (2022).
22. Kart, T. *et al.* Deep learning-based automated abdominal organ segmentation in the UK Biobank and German National Cohort Magnetic Resonance Imaging Studies. *Investigative Radiology* **56**, 401–408 (2021).

23. Ji, Y. *et al.* Amos: A large-scale abdominal multi-organ benchmark for versatile medical image segmentation. *Advances in neural information processing systems* **35**, 36722–36732 (2022).
24. Virtanen, P. *et al.* SciPy 1.0: fundamental algorithms for scientific computing in Python. *Nature methods* **17**, 261–272 (2020).
25. Kofler, F. *et al.* Panoptica – instance-wise evaluation of 3D semantic and instance segmentation maps. (2023).
26. D'Antonoli, T. A. *et al.* TotalSegmentator MRI: Sequence-Independent Segmentation of 59 Anatomical Structures in MR images. *arXiv preprint arXiv:2405.19492* (2024).
27. Häntze, H. *et al.* MRSegmentator: Robust Multi-Modality Segmentation of 40 Classes in MRI and CT Sequences. *arXiv preprint arXiv:2405.06463* (2024).
28. Zhuang, Y. *et al.* MRISegmentator-Abdomen: A Fully Automated Multi-Organ and Structure Segmentation Tool for T1-weighted Abdominal MRI. *arXiv preprint arXiv:2405.05944* (2024).
29. Somasundaram, A. *et al.* Evaluating Sex-specific Differences in Abdominal Fat Volume and Proton Density Fat Fraction on MRI Scans Using Automated nnU-Net-based Segmentation. *Radiology: Artificial Intelligence* **0**, e230471.

Tables

Table 1: List of classes in our TotalVibeSegmentator and the public facing TotalSegmentator (version 2) for CT images. * indicates that we excluded the value for the aggregated results as the reference standard is different. N/A: Not available

Label name	Grouping	This study	Akinci D'Antonoli et Al.	Häntze et Al.
femur left	bone	0.97 CI: [0.97-0.97]	0.84 CI: [0.83-0.85]	0.81 CI: [0.81-0.82]
femur right	bone	0.97 CI: [0.96-0.97]	0.84 CI: [0.83-0.85]	0.83 CI: [0.82-0.83]
hip left	bone	0.96 CI: [0.95-0.96]	0.66 CI: [0.64-0.68]	0.74 CI: [0.73-0.75]
hip right	bone	0.96 CI: [0.95-0.96]	0.62 CI: [0.59-0.64]	0.74 CI: [0.73-0.75]
humerus left	bone	0.95 CI: [0.93-0.96]	0.72 CI: [0.71-0.74]	N/A
humerus right	bone	0.94 CI: [0.93-0.95]	0.73 CI: [0.72-0.74]	N/A
sacrum	bone	0.96 CI: [0.96-0.96]	N/A	0.73 CI: [0.71-0.74]
duodenum	digestion organ	0.87 CI: [0.84-0.90]	0.53 CI: [0.45-0.61]	0.63 CI: [0.58-0.68]
esophagus*	digestion organ	0.90 CI: [0.89-0.91]	0.49 CI: [0.44-0.53]	0.50 CI: [0.44-0.55]
intestine	digestion organ	0.93 CI: [0.93-0.94]	0.65 CI: [0.61-0.69]	N/A
stomach	digestion organ	0.90 CI: [0.87-0.92]	0.83 CI: [0.80-0.85]	0.82 CI: [0.79-0.86]
gluteus maximus left	muscle	0.98 CI: [0.98-0.98]	0.71 CI: [0.68-0.73]	0.78 CI: [0.76-0.79]
gluteus maximus right	muscle	0.98 CI: [0.97-0.98]	0.71 CI: [0.69-0.73]	0.79 CI: [0.77-0.80]
gluteus medius left	muscle	0.95 CI: [0.95-0.95]	0.75 CI: [0.74-0.76]	0.78 CI: [0.77-0.80]
gluteus medius right	muscle	0.97 CI: [0.96-0.97]	0.79 CI: [0.78-0.79]	0.83 CI: [0.82-0.83]
gluteus minimus left	muscle	0.94 CI: [0.93-0.95]	0.54 CI: [0.51-0.56]	0.58 CI: [0.55-0.61]
gluteus minimus right	muscle	0.94 CI: [0.93-0.95]	0.57 CI: [0.54-0.60]	0.60 CI: [0.56-0.64]
iliopsoas left	muscle	0.96 CI: [0.96-0.97]	0.80 CI: [0.78-0.82]	0.73 CI: [0.70-0.75]
iliopsoas right	muscle	0.96 CI: [0.96-0.97]	0.76 CI: [0.73-0.78]	0.69 CI: [0.64-0.74]
gallbladder	organ	0.85 CI: [0.80-0.88]	0.47 CI: [0.30-0.62]	0.61 CI: [0.48-0.72]
heart	organ	0.97 CI: [0.96-0.97]	0.87 CI: [0.85-0.88]	0.87 CI: [0.86-0.89]
kidney left	organ	0.92 CI: [0.91-0.93]	0.88 CI: [0.86-0.89]	0.92 CI: [0.91-0.93]
kidney right	organ	0.92 CI: [0.90-0.94]	0.86 CI: [0.84-0.88]	0.91 CI: [0.89-0.93]
liver	organ	0.97 CI: [0.97-0.98]	0.90 CI: [0.89-0.91]	0.95 CI: [0.94-0.95]
lung left	organ	0.96 CI: [0.96-0.97]	0.91 CI: [0.89-0.94]	0.92 CI: [0.90-0.93]
lung right	organ	0.97 CI: [0.96-0.97]	0.92 CI: [0.90-0.94]	0.92 CI: [0.90-0.94]
pancreas	organ	0.89 CI: [0.86-0.91]	0.50 CI: [0.41-0.58]	0.71 CI: [0.67-0.76]
prostate	organ	0.94 CI: [0.93-0.95]	0.67 CI: [0.60-0.74]	N/A
spleen	organ	0.94 CI: [0.93-0.94]	0.89 CI: [0.88-0.90]	0.92 CI: [0.91-0.94]
urinary bladder	organ	0.95 CI: [0.93-0.96]	0.81 CI: [0.75-0.87]	0.85 CI: [0.81-0.89]
IVD	spine	0.90 CI: [0.89-0.91]	0.61 CI: [0.58-0.64]	0.74 CI: [0.70-0.78]
spinal cord	spine	0.89 CI: [0.88-0.91]	0.31 CI: [0.29-0.33]	N/A
vertebra body	spine	0.94 CI: [0.93-0.94]	0.77 CI: [0.76-0.78]	0.72 CI: [0.70-0.74]
adrenal gland left	gland	0.84 CI: [0.82-0.86]	0.44 CI: [0.36-0.51]	0.65 CI: [0.58-0.70]
adrenal gland right	gland	0.84 CI: [0.81-0.87]	0.51 CI: [0.46-0.57]	0.61 CI: [0.56-0.66]
aorta	vessel	0.95 CI: [0.95-0.96]	0.63 CI: [0.60-0.66]	0.84 CI: [0.83-0.86]
atrial appendage left	vessel	0.84 CI: [0.81-0.87]	0.64 CI: [0.63-0.66]	0.65 CI: [0.64-0.67]
autochthon left	vessel	0.97 CI: [0.96-0.97]	0.64 CI: [0.63-0.65]	0.65 CI: [0.63-0.67]
iliac artery left	vessel	0.88 CI: [0.86-0.90]	0.53 CI: [0.47-0.58]	0.54 CI: [0.50-0.58]
iliac artery right	vessel	0.86 CI: [0.83-0.89]	0.43 CI: [0.39-0.47]	0.71 CI: [0.67-0.75]
iliac vena left	vessel	0.91 CI: [0.90-0.92]	0.66 CI: [0.61-0.70]	0.72 CI: [0.68-0.76]
iliac vena right	vessel	0.90 CI: [0.89-0.92]	0.63 CI: [0.58-0.69]	0.73 CI: [0.71-0.75]
inferior vena cava	vessel	0.92 CI: [0.91-0.94]	0.48 CI: [0.41-0.56]	N/A
portal vein and splenic vein	vessel	0.82 CI: [0.78-0.85]	0.39 CI: [0.31-0.47]	0.39 CI: [0.36-0.41]
pulmonary vein	vessel	0.91 CI: [0.90-0.92]	0.67 CI: [0.65-0.69]	N/A

Table 2: List of classes in our TotalVibeSegmentator, other MR Torso segmentations and the public facing TotalSegmentator (version 2) for CT images. Available Segmentation are marked with X. Annotation: 1) not available at time or writing 2) Replaced by Vertebra body 3) Merged with small bowel; Now: Intestine, 4) Splitted in lung lobe like the CT version, 5) Not Public; License required.

Name	Chirality/Instances	TotalSegmentator (CT)	Ours	Akinci D'Antonoli et Al.	Häntze et Al.	Zhuang et Al. 1)
Spleen		X	X	X	X	X
Kidney	Left, Right	X	X	X	X	X
Gallbladder		X	X	X	X	X
Liver		X	X	X	X	X
Stomach		X	X	X	X	X
Pancreas		X	X	X	X	X
Adrenal gland	Left, Right	X	X	X	X	X
Lung	Left, Right	X 4)	X 4)	X	X	X
Esophagus		X	X	X	X	X
Trachea		X	X	-	-	-
Thyroid gland		X	X	-	-	-
Small bowel		X	X 3)	X	X	X
Duodenum		X	X	X	X	X
Colon		X	X 3)	X	X	X
Urinary bladder		X	X	X	X	-
Prostate		X	X	X	-	-
Kidney cyst	Left, Right	X	-	-	-	-
Sacrum		X	X	X	X	X
Vertebrae	C1-L5, S1	X	2)	2)	2)	X [T7 – L5]
Heart		X	X	X	X	-
Aorta		X	X	X	X	X
Inferior vena cava		X	X	X	X	X
Brachiocephalic trunk		X	X	-	-	-
Subclavian artery	Left, Right	X	X	-	-	-
Common carotid artery	Left, Right	X	X	-	-	-
Brachiocephalic vein	Left, Right	X	X	-	-	-
Atrial appendage left		X	X	-	-	-
Superior vena cava		X	X	-	-	-
Inferior vena cava		X	X	-	-	-
Portal vein and splenic vein		X	X	X	X	X
Iliac artery	Left, Right	X	X	X	X	X
Iliac vena	Left, Right	X	X	X	X	X
Humerus	Left, Right	X	X	X	-	-
Scapula	Left, Right	X	X	-	-	-
Clavicula	Left, Right	X	X	-	-	-
Femur	Left, Right	X	X	X	X	-
Hip	Left, Right	X	X	X	X	X
Spinal cord		X	X	-	-	-
Gluteus maximus	Left, Right	X	X	X	X	X
Gluteus medius	Left, Right	X	X	X	X	X
Gluteus minimus	Left, Right	X	X	X	X	-
Autochthon	Left, Right	X	X	X	X	X
Iliopsoas	Left, Right	X	X	X	X	X
Brain		X	-	-	-	-
Skull		X	-	-	-	-
Rib	[Left, Right] × 12	X	-	-	-	X [4-12]
Sternum		X	X	-	-	-
Costal artilages		X	X	-	-	-
subcutaneous_fat		-	X	5)	-	-
Muscle (other/body composition)		-	X	5)	-	-
Inner fat		-	X	5)	-	-
IVD		-	X	-	-	-
Vertebra body		-	X	X	X	-
Vertebra posterior elements		-	X	-	-	-
Spinal channel		-	X	-	-	-
Fibula		-	-	X	-	-
Tibia		-	-	X	-	-
Upper Leg Muscles	4 Groups × [Left, Right]	-	-	X	-	-

Acknowledgements - Funding

The research for this article received funding from the European Research Council (ERC) under the European Union's Horizon 2020 research and innovation program (101045128—iBack-epic—ERC2021-COG).

This project was conducted with data from the German National Cohort (GNC) (www.nako.de). The GNC is funded by the Federal Ministry of Education and Research (BMBF) [project funding reference numbers: 01ER1301A/B/C and 01ER1511D], federal states and the Helmholtz Association with additional financial support by the participating universities and the institutes of the Leibniz Association. We thank all participants who took part in the GNC study and the staff in this research program.

This research has been conducted using the UK Biobank Resource under Application Number 87802

Supplements

Segmentation Process – Initial Torso Segmentation

For the initial segmentation of four full-torso NAKO images (2 male, 2 female), three segmentation networks are employed. The body composition network from Jung et al.¹ is utilized to segment subcutaneous fat, muscle (general), and body fat. The intermuscular fat tissue was merged with muscle tissue because differentiating between them is out of the scope of this work. We extended the segmentations to also include the arms, legs and parts of the shoulder area. Existing segmentations helped us to delineate the remaining missing structures more easily. Each VIBE consists of four images: in-phase, out-of-phase, water, and fat. TotalSegmentator (public version 2)² is used to generate organs, vessels, and specific muscle segmentations on manipulated water images. Given the rough linear correlation between organ water content and CT attenuation, the water images are manipulated to facilitate segmentation by TotalSegmentator. We used the body composition segmentation to reduce

the muscle signal by 20 % in the water image; we selected the background and lung in the in-phase image by thresholding and connected component analysis and subtracted these masks with a value of 600 in the water image. Following this approach, most soft tissue could be segmented with only small errors. These values were determined manually to make the VIBE water image close enough for the segmentation network to not vastly under-segment the lungs, muscles, and liver in the four initial images. Due to signal shifts, these metrics are not generally applicable to all water images. This process could not produce certain structures such as bone, colon, portal and splenic vein, thyroid gland, spinal cord, and costal cartilage, which were manually segmented. Spine segmentation is derived from aligned T2w sagittal images with SPINEPS^{3,4}, resampled to match the VIBE. We observed that multiple structures are poorly visible in UKBB. This increased the annotation time, therefore we decided to keep the number of UKBB images low and focused more on NAKO images.

Spine Instance Segmentation

The TotalSegmentator² and SPINEPS^{3,4} papers highlighted nnUNet's⁷ patch-wise inference limitations, which could cause off-by-one errors and vertebra merging, making it less suitable for instance segmentation. Moreover, adding approximately 25 vertebra classes increased the system requirements to run the algorithm. Despite these challenges, fast instance segmentation remained valuable for researchers and medical professionals. To address this, we trained a separate instance network, where we expected these issues to remain. In the future, these issues could be solved by specialized networks. SPINEPS⁴ already solved the merging issue with its two-step approach but could not yet label the vertebra to their class and naively counted from top to bottom.

For the spine, we used aligned T2-weighted turbo spin echo images with the VIBE. Instance labels were defined by counting from the neck downwards in the T2-weighted images. For training, we resampled 2000 instance segmentations from T2-weighted turbo spin echo to VIBE. The predictions from the resulting segmentation model smoothed step-shape interpolation errors and visually appeared more accurate than the original training data. As

previously noted in the literature^{2,4,8}, this method was prone to instability, resulting in vertebra labels being offset by one, and occasionally, a single vertebra was labeled as two different vertebra IDs, dividing it. We omitted an evaluation for three reasons: this served as a stopgap for users interested in the rough location of the vertebra level, we currently had no ground truth for spine segmentation on VIBE, and a proper instance segmentation would require another model than nnUNet that prevents off-by-one errors and vertebra merging.

Training the nnUNet

Other papers^{2,4,9} noted a left-right structure issue with nnUNet⁷. We turn off random flipping during training, to address this swapping in our nnUNet training. Moreover, we employ elastic deformation¹⁰ to generate additional training images, increasing the dataset size by a factor of 4-500, depending on how many ground truths we had.

The segmentation model is trained with random initialization on a single input image out of water, in-phase, or out-of-phase contrast. For new training segmentations of the three outputs were merged into a single segmentation. We remove connected components smaller than a specific volume threshold for each organ. If an organ only consists of one tightly packed connected component, we discard all components except the largest. Prioritization during merging focuses on structures prone to under-segmentation, with lower priority segmentations only added to unoccupied voxels. This computer-intensive process aids in eliminating small false positives and underpredictions, particularly for vessels. With the model trained on 79 or more subjects, this step is no longer needed to prevent common under-segmentation. We have rewritten the inference code of nnUNet. The large number of classes and image size lead to a considerable slowdown in the original implementation. The rewritten code frees the GPU memory earlier and is faster.

To increase generalizability, we resampled other sequences available in NAKO, such as T2w haste (torso), proton density (pelvis), 6-point Dixon (lower torso), and sagittal T2w turbo spin echo (spine) to the spacing of the VIBE images to 1.4 mm in the axial plane and 3 mm in the superior-inferior direction. We manually removed all samples with motion artifacts. The

remaining sequences were used for training after we achieved ten corrected subjects. For the final training we looked at all other sequences and removed images with delineation errors or repaired small issues. Additionally, for the final iteration we selected 40 images where our previous segmentation disagreed with Kart et al.^{5,6}, those were images mostly with cysts, enlarged organs and image artifacts. This step was intended to improve the behavior of those pathologies.

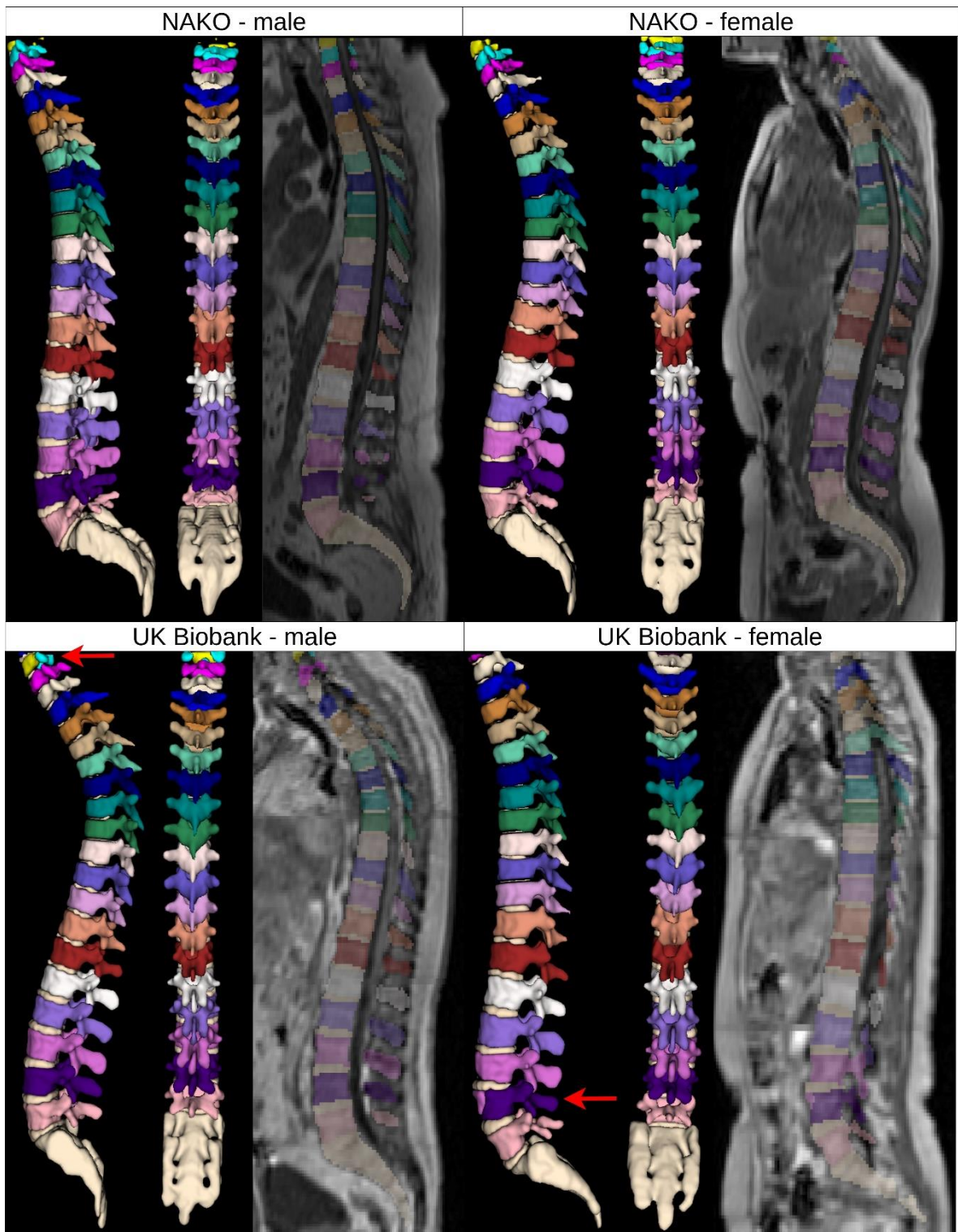


Figure Supplement 1: Spine instance segmentation. One the NAKO vibs off-by-one errors are rare. For out-of-distribution like the UKBB vertebra merging and off-by-one errors are common. We marked two examples with a red arrow.

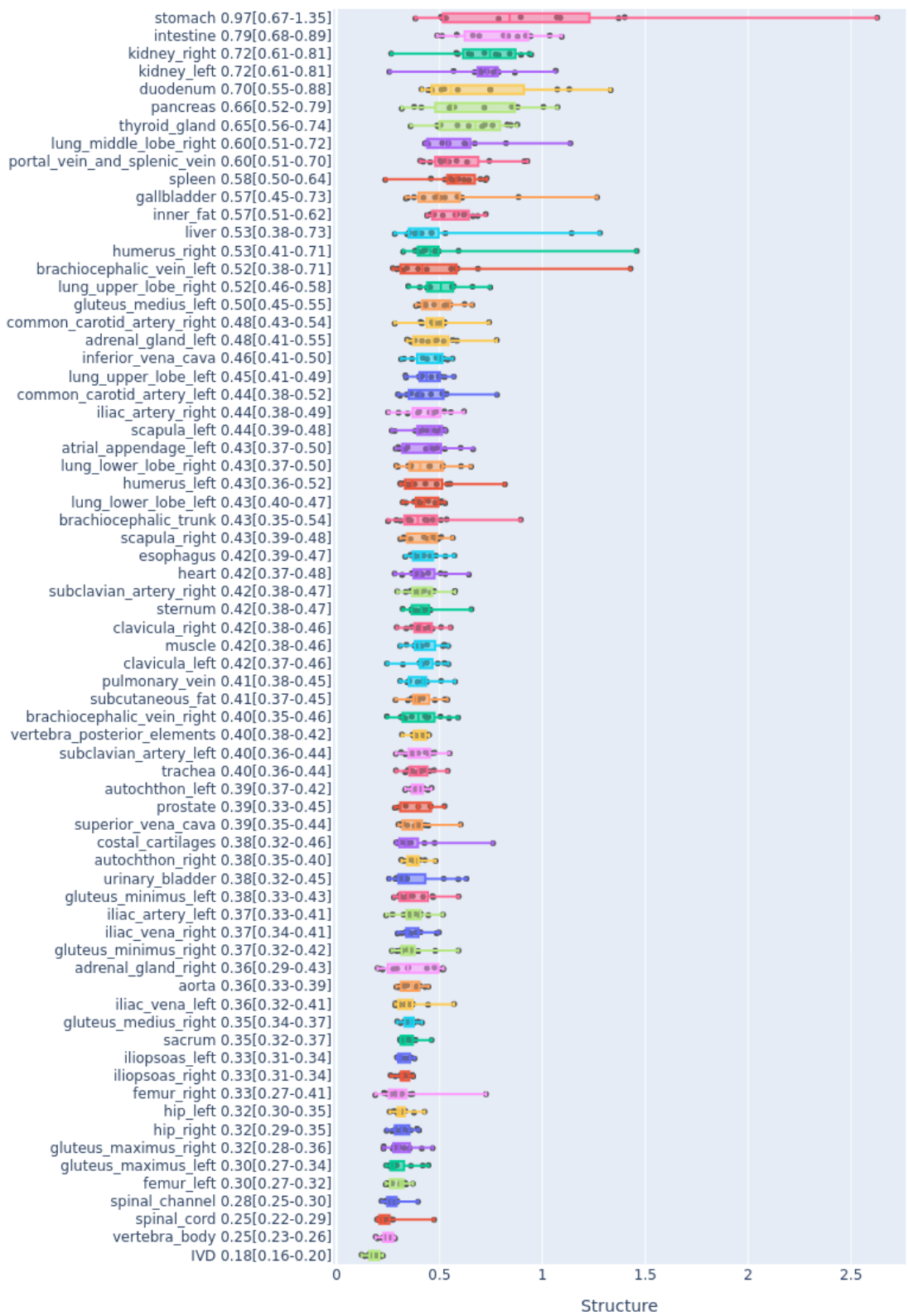


Figure Supplement 2: Average Symmetric Surface Distance in mm (lower is better) over all classes compared on repaired and predicted Volumetric Interpolated Breath-hold Examination (VIBE) on the 12 NAKO and UK Biobank images.

References

1. Jung, M. *et al.* Deep learning to predict mortality from whole-body magnetic resonance imaging in the general population.
2. Wasserthal, J. *et al.* Totalsegmentator: Robust segmentation of 104 anatomic structures in ct images. *Radiology: Artificial Intelligence* **5**, (2023).
3. Graf, R. *et al.* Denoising diffusion-based MRI to CT image translation enables automated spinal segmentation. *European Radiology Experimental* **7**, 70 (2023).
4. Möller, H. *et al.* SPINEPS—Automatic Whole Spine Segmentation of T2-weighted MR images using a Two-Phase Approach to Multi-class Semantic and Instance Segmentation. *arXiv preprint arXiv:2402.16368* (2024).
5. Kart, T. *et al.* Automated imaging-based abdominal organ segmentation and quality control in 20,000 participants of the UK Biobank and German National Cohort Studies. *Scientific Reports* **12**, 18733 (2022).
6. Kart, T. *et al.* Deep learning-based automated abdominal organ segmentation in the UK Biobank and German National Cohort Magnetic Resonance Imaging Studies. *Investigative Radiology* **56**, 401–408 (2021).
7. Isensee, F., Jaeger, P. F., Kohl, S. A., Petersen, J. & Maier-Hein, K. H. nnU-Net: a self-configuring method for deep learning-based biomedical image segmentation. *Nature methods* **18**, 203–211 (2021).
8. van der Graaf, J. W. *et al.* Lumbar spine segmentation in MR images: a dataset and a public benchmark. *Scientific Data* **11**, 264 (2024).
9. Häntze, H. *et al.* MRSegmentator: Robust Multi-Modality Segmentation of 40 Classes in MRI and CT Sequences. *arXiv preprint arXiv:2405.06463* (2024).
10. Ronneberger, O., Fischer, P. & Brox, T. U-net: Convolutional networks for biomedical image segmentation. in *Medical Image Computing and Computer-Assisted Intervention--MICCAI 2015: 18th International Conference* 234-241. https://doi.org/10.1007/978-3-319-24574-4_28 (Springer, 2015). doi:https://doi.org/10.1007/978-3-319-24574-4_28.